Finite-difference time-domain synthesis of infrasound propagation through an absorbing atmosphere

C. de Groot–Hedlin
Scripps Institution of Oceanography, University of California, San Diego, La Jolla, California 92093

(Received 5 June 2007; revised 16 June 2008; accepted 18 June 2008)

Equations applicable to finite-difference time-domain (FDTD) computation of infrasound propagation through an absorbing atmosphere are derived and examined in this paper. It is shown that over altitudes up to 160 km, and at frequencies relevant to global infrasound propagation, i.e., 0.02–5 Hz, the acoustic absorption in dB/m varies approximately as the square of the propagation frequency plus a small constant term. A second-order differential equation is presented for an atmosphere modeled as a compressible Newtonian fluid with low shear viscosity, acted on by a small external damping force. It is shown that the solution to this equation represents pressure fluctuations with the attenuation indicated above. Increased dispersion is predicted at altitudes over 100 km at infrasound frequencies. The governing propagation equation is separated into two partial differential equations that are first order in time for FDTD implementation. A numerical analysis of errors inherent to this FDTD method shows that the attenuation term imposes additional stability constraints on the FDTD algorithm. Comparison of FDTD results for models with and without attenuation shows that the predicted transmission losses for the attenuating media agree with those computed from synthesized waveforms. © *2008 Acoustical Society of America.*
[DOI: 10.1121/1.2959736]

PACS number(s): 43.28.Dm, 43.28.Js, 43.20.Hq [VEO] Pages: 1430–1441

I. INTRODUCTION

Ever since pressure fluctuations generated by the 1883 explosion of Krakatoa were recorded on barometers throughout the US, Europe, and Russia (Bass *et al.*, 2006), it has been understood that volcanoes excite infrasonic waves—subaudible acoustic energy—detectable at ranges from hundreds to thousands of kilometers. Over the years, pressure waves generated by both earthquakes and volcanoes have been detected at distances of hundreds to thousands of kilometers from the source regions (e.g., Mikumo, 1968; Wilson and Forbes, 1969; Young and Greene, 1982). Currently, a global infrasound network consisting of 60 infrasound stations distributed over the Earth is being deployed as one part of the International Monitoring System (IMS) designed to detect nuclear explosions (Der *et al.*, 2002). The construction of this network of stations, which measure differential pressure in the frequency range from roughly 0.02 to 5 Hz (e.g., Arrowsmith and Hedlin, 2005), has allowed infrasound to emerge as a method of investigating a much broader range of atmospheric and geophysical phenomena than was possible until now. Recent work has focused on such disparate infrasound sources as meteors (ReVelle *et al.*, 2004), ocean swells (Garceś *et al.*, 2004a), surf noise (Arrowsmith and Hedlin, 2005), and tsunamis (Le Pichon *et al.*, 2005), as well as the tragic Columbia shuttle explosion (Garceś *et al.*, 2004b). In other studies, seasonal variations in infrasound arrivals from recurring sources were used to probe atmospheric properties (e.g., Le Pichon *et al.*, 2002; Garceś *et al.*, 2004a). However, improvements are needed in both atmospheric models and acoustic propagation modeling methods in order to correctly interpret the wide range of signals detected by the global infrasound network (Bass *et al.*, 2006).

Infrasound propagation is controlled mainly by reflections by the ground terrain, scattering by atmospheric turbulence, advection through a windy atmosphere, refraction due to sound-speed gradients, and attenuation due to the absorbing properties of the atmosphere. Infrasound detections at long ranges from the source are generally either thermospheric arrivals, which result from downward refraction by the steep temperature gradients of the upper atmosphere, or stratospheric arrivals, which are ducted between the ground and the stratopause. Detection of the latter depends strongly on the stratospheric winds, while thermospheric waves are strongly attenuated due to enhanced atmospheric absorption within the thermosphere. Finite-difference time-domain (FDTD) methods have been developed to model the effects of sound propagation in a windy atmosphere (e.g., Ostashev *et al.*, 2005). The goal of the present study is to develop a FDTD method of simulating infrasound propagation through a heterogeneous, absorptive atmosphere.

The effects of absorption are usually simulated using frequency-domain modeling techniques, such as parabolic equation (PE) or fast field program (FFP) methods (e.g., Jensen *et al.*, 1994). These methods use a heuristic approach of adding a small imaginary value to the acoustic velocity to simulate attenuation. However, these frequency-domain methods make use of approximations to the atmospheric model and/or to the governing wave equation that limit their applicability. For instance, FFP methods assume that material properties of the model vary only in a single spatial coordinate, while PE methods compute one-way propagation, which is valid only for models with limited range dependence.

By contrast, the FDTD approach is applicable to a wide range of complicated phenomena in heterogeneous media as

it relies on a discretization of the governing equations. The wider applicability of the FDTD method comes at the cost of greater computational time and memory requirements. However, with advances in computing technology, the FDTD method has drawn greater interest. A method of incorporating attenuation into an FDTD approach was developed by Day and Minster (1984) for anelastic media, with refinements by Emmerich and Korn (1987), Blanch *et al.* (1995), and Day (1998). These methods approximate the frequency-domain stress-strain relations by low-order rational functions of frequency. The approach may be applied to many types of anelastic media. However, a drawback is that this approach is computationally time- and memory-intensive as compared to nonabsorptive materials.

In the next section, sound absorption mechanisms within the atmosphere are described. It is shown that at frequencies relevant to global infrasound investigations, i.e., 0.02–5 Hz, the attenuation coefficient (in dB/m) can be decomposed into two parts: a constant term and another proportional to the square of the frequency. In Sec. III, it is demonstrated that these attenuation effects may be simulated by modifying the wave equation to include two attenuation terms. The degree to which the revised wave equation introduces material dispersion is examined over the infrasound frequency bandwidth for realistic attenuation values. In Sec. IV, two sets of partial differential equations that are first order in time are introduced to replace the attenuating wave equation. A numerical algorithm to implement these FDTD equations is developed for the case of two-dimensional (2D) models. It is shown that inclusion of an attenuation term proportional to the square of the frequency imposes additional constraints on the model discretization in order to maintain numerical stability. In Sec. V, the algorithm is applied to several environmental models, and FDTD solutions computed with and without atmospheric absorption are compared. The paper concludes with a discussion and summary of results.

II. ATMOSPHERIC ABSORPTION OF SOUND

The absorption of sound within any gas is controlled primarily by the composition of the gas mixture, the ambient pressure, temperature, sound frequency and, at higher frequencies, by the humidity (Bass *et al.*, 1995; Dain and Lueptow, 2001; Sutherland and Bass, 2004). Absorption mechanisms can be categorized in terms of classical losses caused by the irreversible transfer of the kinetic energy of the acoustic wave into heat, and molecular relaxation losses, which involve the excitation of the energy states of the gas molecules comprising the atmosphere (Evans *et al.*, 1972; Ejakov *et al.*, 2003). Classical absorption includes losses due to diffusion, heat conduction, and viscosity; molecular relaxation losses must be computed for each of the primary gas constituents in the air–O_2, N_2, CO_2, and O_3. The absorption mechanisms are cumulative, thus, the total attenuation coefficient of sound, in dB/m, is given by the linear sum of the attenuation components associated with each individual loss mechanism.

Attenuation coefficients computed using the expressions given in Sutherland and Bass (2004, 2006) are shown as a function of altitude for frequencies ranging from 0.05–4 Hz in Fig. 1(a). A simplified form of the attenuation coefficient is sought as a function of frequency at each altitude for the purpose of accurately including attenuation effects within the finite-difference computations. For infrasonic frequencies, classical losses dominate at altitudes above approximately 60 km, and the associated attenuation coefficient, in dB/m, is proportional to the square of the frequency (Sutherland and Bass, 2004). At lower altitudes, losses associated with excitation of vibrational modes of the gas molecules dominate. For each of the gas constituents in the air, these losses, $q_{\mathrm{vib},i}$ are proportional to

$$\frac{(f^2/f_{\mathrm{vib},i})}{[1+(f/f_{\mathrm{vib},i})^2]c} \tag{1}$$

(Sutherland and Bass, 2004), where f is the sound frequency, $f_{\mathrm{vib},i}$ is the relaxation frequency for a particular gas component, and c is the sound speed in the absence of attenuation. The attenuation coefficient associated with the excitation of the vibrational modes of each component of the gas, in dB/m, is thus approximately proportional to the square of the frequency at low frequencies $f \ll f_{\mathrm{vib},i}$, and is nearly a constant at high frequencies $f \gg f_{\mathrm{vib},i}$.

The attenuation curves of Fig. 1(a) suggest that the cumulative attenuation coefficient q, expressed in dB/m, may be approximated by decomposing it into a component proportional to the square of the frequency plus a constant at

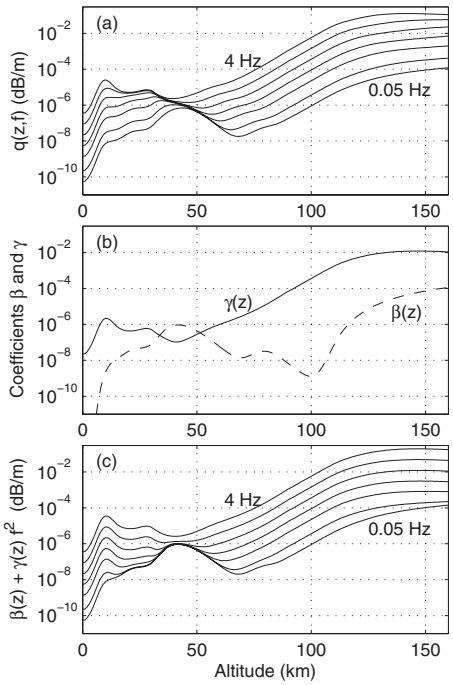

FIG. 1. (a) Attenuation coefficients $q(z,f)$ for frequencies of 0.05 (lowest curve), 0.1, 0.25, 0.5, 1, 2, and 4 Hz (uppermost curve), computed using the expressions given in Sutherland and Bass (2004). (b) Decomposition of the attenuation coefficients at each altitude in terms of a frequency-independent component $\beta(z)$, shown by the dashed line, and a component of the attenuation $\gamma(z)$ proportional to f^2, shown by the solid line; $\beta(z)$ is in units of m^{-1}, γ has units of $\mathrm{s}^2\,\mathrm{m}^{-1}$. Since the decomposition is imprecise, the coefficients depend on the bandwidth chosen; values shown here are derived for the frequency range from 0.05–4 Hz shown in (a). (c) Attenuation curves reconstructed using $\beta(z)+\gamma(z)f^2$.

each altitude, although the fit may be degraded where vibrational losses dominate, as discussed above. Accordingly, the coefficients β and γ that yielded the least-squares best fit to $q(z,f)=\beta(z)+\gamma(z)f^2$ were computed at each altitude. The result of this decomposition for the frequency range 0.05–4 Hz is shown in Fig. 1(b); the solid line shows the derived $\gamma(z)$ attenuation coefficients and the dashed line indicates $\beta(z)$. The attenuation curves in Fig. 1(c) were computed using $\beta(z)+\gamma(z)f^2$; comparison with the curves in Fig. 1(a) indicates the degree of accuracy of this approximation over the frequency bandwidth relevant to infrasound propagation. Discrepancies in the fit are most noticeable at the lower altitudes. Since attenuation is almost negligible within the lower atmosphere—an attenuation coefficient of 10^{-6} dB/m corresponds to a 0.1-dB loss over a 100-km path length—these small errors are insignificant. The misfit between attenuation values shown in Fig. 1(a) and Fig. 1(b) approach 20–30% at altitudes over 120 km. However, attenuation estimates are only approximate at altitudes greater than 90 km due to uncertainties in the atmospheric composition (Sutherland and Bass, 2004). A misfit up to 30% may thus be considered sufficient, given that the attenuation spans many orders of magnitude over the infrasound propagation band.

As indicated in Fig. 1(c), the derived attenuation coefficients $\beta(z)+\gamma(z)f^2$ dB/m are reasonably accurate over approximately two orders of magnitude in frequency. However, these coefficients must be rederived for any other frequency band of interest since the decomposition is inexact. In general, the constant term $\beta(z)$ is larger and the $\gamma(z)$ term is smaller for higher frequency bands.

III. ATMOSPHERIC ABSORPTION AND VELOCITY DISPERSION

Given that the atmospheric absorption of sound may be approximated by an attenuation coefficient with two terms—a constant plus a term proportional to the square of the frequency—an acoustic plane wave propagating in the positive x direction must have pressure fluctuations of the form

$$p(x,t) \propto e^{i2\pi f(x/c_p - t)} e^{-\alpha(f)x}, \tag{2}$$

where c_p is the phase speed, t is time, and the attenuation $\alpha=q/(20\log_{10}(e))$ is a scaled version of the attenuation defined in the previous section.

It will now be shown that the solution to the following equation has the form given by Eq. (2) for the attenuation values and frequencies considered in this paper:

$$c^2\left(1+\mu\frac{\partial}{\partial t}\right)\frac{\partial^2 p}{\partial x^2} = \frac{\partial^2 p}{\partial t^2} + \xi\frac{\partial p}{\partial t}, \tag{3}$$

where μ is the shear viscosity, in units of seconds, and ξ is a damping coefficient, in units of s^{-1}. As outlined in the Appendix (for a 3D medium), this equation describes plane-wave propagation though a homogeneous compressible Newtonian fluid with a small external damping force. The case $\mu\neq 0$, $\xi=0$ is a medium in which internal viscosity is the dominant absorption mechanism (Knopoff, 1956; Lighthill, 1978). For the case $\mu=0$, $\xi\neq 0$, Eq. (3) corresponds to a simple damped oscillator, with a viscous force proportional to the particle velocity opposing the motion (e.g., Boyce and di Prima, 1977). The latter case reduces to the telegraph equation, which combines the wave equation and the diffusion equation. Here, we treat only the case $\xi\partial p/\partial t \ll \partial^2 p/\partial t^2$ so that wave motion dominates, not diffusion.

Inserting a trial solution of the form $p(x,t)=e^{i(kx-\omega t)}$ into Eq. (3), where ω is the circular frequency and k is the wavenumber, yields a complex-valued (squared) wavenumber of the form

$$k^2(\omega) = \frac{1}{c^2}\frac{\omega^2+i\xi\omega}{(1-i\mu\omega)}. \tag{4}$$

From Eq. (2), it can be seen that the wavenumber k is related to the frequency-dependent phase speed $c_p(\omega)$ and attenuation through

$$k = \omega/c_p(\omega) + i\alpha(\omega). \tag{5}$$

By writing $k^2(\omega)$ in exponential notation as $k^2(\omega)=|k^2|\exp(i\phi)$, where ϕ is the argument of $k^2(\omega)$, and applying Eq. (5), it can be seen that

$$\omega/c_p(\omega) = \mathrm{Re(k)} = \sqrt{|k^2|}\cos(\phi/2), \tag{6a}$$

$$\alpha(\omega) = \mathrm{Im}(k) = \sqrt{|k^2|}\sin(\phi/2). \tag{6b}$$

With some algebra manipulations, and applying trigonometric half-angle formulas, it can be shown that

$$\left(\frac{c_p(\omega)}{c}\right)^2 = \frac{2(1+\mu^2\omega^2)}{(1-\mu\xi)+\sqrt{(1+(\xi/\omega)^2)(1+\mu^2\omega^2)}}, \tag{7a}$$

and

$$\alpha^2(\omega) = \frac{\omega^2}{2c^2(1+\mu^2\omega^2)}\left[\sqrt{(1+(\xi/\omega)^2)(1+\mu^2\omega^2)} - (1-\mu\xi)\right]. \tag{7b}$$

Thus, the solution to Eq. (3) is

$$p(x,t) = e^{i\omega(x/c_p(\omega)-t)}e^{-\alpha(\omega)x}, \tag{8}$$

where $c_p(\omega)$ and $\alpha(\omega)$ are the positive square roots of Eqs. (7a) and (7b), respectively, for plane waves propagating in the positive x direction.

For small viscosity coefficients, i.e., $\xi \ll \omega$ and $\mu\omega \ll 1$, and retaining terms up to second order in (ξ/ω) and $\mu\omega$, it can be shown that $\alpha^2(\omega)\approx(\xi+\mu\omega^2)^2/(4c^2)$, so

$$\alpha(\omega) \approx (\xi+\mu\omega^2)/(2c), \tag{9}$$

which has the desired response for acoustic propagation through an absorbing atmosphere. Comparing Eqs. (2) and (9), the coefficient of viscosity μ is related to γ through

$$\mu = \gamma c/(40\pi^2\log_{10}(e)). \tag{10a}$$

and the damping coefficient ξ relates to β as

$$\xi = c\beta/(10\log_{10}(e)). \tag{10b}$$

These values are dependent on altitude, as both c and the attenuation coefficients γ and β vary with altitude. Coeffi-

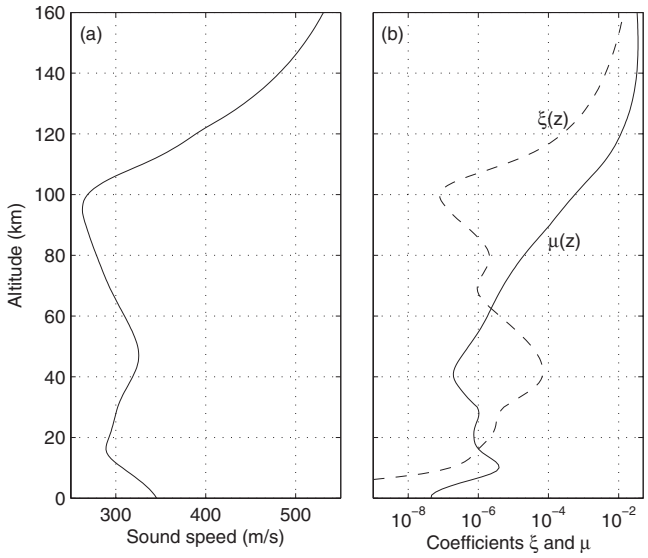

FIG. 2. (a) Sound velocity profile. (b) Coefficients $\xi(z)$ (dashed line, in units of s^{-1}) and $\mu(z)$ (solid line, in units of seconds) corresponding to the given sound velocity profile, and to the coefficients $\beta(z)$ and $\gamma(z)$, shown in Fig. 1(b).

cients $\mu(z)$ and $\xi(z)$ are shown in Fig. 2(b) for the sound velocity profile shown in Fig. 2(a). These coefficients are used in the remainder of this paper to designate realistic atmospheric attenuation value.

Equation (7a) indicates that the acoustic velocity is dispersive; this is in agreement with the Kramers-Kronig relations, initially developed in electromagnetic theory, which show that phase velocity shows frequency dependence in attenuating media. The relation between attenuation and dispersion for acoustic waves in media with attenuation obeying other frequency power laws in discussed in Aki and Richards (1980). More recently, Bass *et al.* (2007) examined the effect of velocity dispersion on sound refraction in the upper atmosphere. Figure 3 shows the derived $c_p(f)/c$ ratios at altitudes of 100, 120, 140, and 160 km for frequencies from 0.01 to 2 Hz, derived using Eq. (7a) and attenuation values shown in Fig. 2(b). These are compared to corresponding

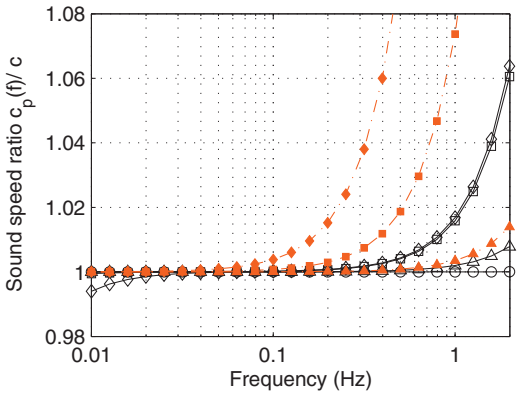

FIG. 3. Ratios of c_p/c as a function of frequency at altitudes of 100 km (circles), 120 km (triangles), 140 km (squares), and 160 km (diamonds). The black lines with open symbols indicate ratios computed using Eq. (7a); the red dash-dot lines with filled symbols indicate corresponding values for 120, 140, and 160 km, computed using a formula from Bass *et al.* (2007). The values of c at these altitudes are shown in Fig. 2(a). At these frequencies, velocity dispersion is significant only at altitudes over 100 km.

ratios computed using formulas found in Bass *et al.* (2007). The results show that dispersion is negligible at altitudes less than 100 km over the range of frequencies typically recorded in global infrasound studies. At higher altitudes, both models indicate significant increases in velocity at the upper end of the infrasound frequency band. However, velocity dispersion at the upper end of the frequency range is more pronounced for the Bass *et al.* (2007) formulas than is predicted by Eq. (7a). It is not clear why this is true. As shown, Eq. (7a) predicts a slight decrease in phase velocity at the lower end of the frequency band at an altitude of 160 km.

IV. ACOUSTIC PROPAGATION IN AN ABSORBING ATMOSPHERE

A. First-order differential equations

As shown in Eqs. (A7), (A85), and (A18) of the Appendix, the following pair of first-order differential equations in time governs linear acoustic propagation through an attenuating atmosphere:

$$\frac{\partial \mathbf{v}_s}{\partial t} = \mathbf{f}_i - \frac{1}{\rho}\left[\nabla p_s - (3\rho c^2/4)\mu\left(\nabla^2 \mathbf{v}_s + \frac{1}{3}\nabla(\nabla \cdot \mathbf{v}_s)\right)\right] - \xi \mathbf{v}_s, \tag{11a}$$

$$\frac{\partial p_s}{\partial t} = -\rho c^2 \nabla \cdot \mathbf{v}_s, \tag{11b}$$

where p_s is defined as the pressure perturbation due to the sound wave, $\mathbf{v}_s$ is the acoustic particle velocity, and ρ is the atmospheric density. The addition of the ξ term is heuristic, added only to yield more realistic atmospheric absorption values. Terms proportional to gravity are important at very low frequencies corresponding to internal waves (Ostashev *et al.*, 2005; Lingevitch *et al.*, 1999) and are omitted here. The effects of wind are beyond the scope of this paper. As expected, Eqs. (11) reduce to the standard FDTD equations for acoustic propagation (Botteldooren, 1994) for the case $\mu=\xi=0$.

As shown in Eq. (A17) in the Appendix, the coupled equations yield

$$\frac{\partial^2 p_s}{\partial t^2} = c^2\left(1 + \mu\frac{\partial}{\partial t}\right)\nabla^2 p_s - \xi\frac{\partial p_s}{\partial t} - \frac{c^2}{\rho}\nabla\rho\cdot\nabla p_s, \tag{12}$$

where the external force has been omitted. For a homogeneous medium, this reduces to

$$\frac{\partial^2 p_s}{\partial t^2} = c^2\left(1 + \mu\frac{\partial}{\partial t}\right)\nabla^2 p_s - \xi\frac{\partial p_s}{\partial t}. \tag{13}$$

In this case the pressure depends only on the distance from the source. The outgoing solution of Eq. (13) for a point source at the origin is given by the real part of

$$p_s(R,t) = A\frac{e^{i\omega(R/c_p(\omega)-t)}}{R}e^{-\alpha(\omega)R}, \tag{14}$$

where $R=\Sigma(x_i x_i)^{1/2}$ is the distance from the source, A is a complex-valued constant, and $c_p(\omega)$ and $\alpha(\omega)$ are the positive square roots of Eqs. (7a) and (7b), respectively.

B. Propagation through a medium with exponentially decreasing density

Equation (14) holds for an isothermal model with constant density and attenuation values. An analytic expression may also be derived for a somewhat more realistic atmospheric model represented as an isothermal medium with exponentially decreasing density. Using the hydrostatic equation $dp_o/dz=-g\rho$, where p_o is the atmospheric pressure in the absence of a sound wave and g is the acceleration due to gravity, and the ideal gas law $p_o=\rho R_a T$, where T is the temperature in degrees Kelvin and $R_a=287.04\ \mathrm{J\ kg^{-1}\ K^{-1}}$ is the gas constant for dry air, the density gradient with altitude is derived as

$$\frac{\partial\rho(z)}{\partial z}=-\frac{\rho g}{R_a T}, \tag{15}$$

for an isothermal atmosphere. Horizontal density gradients are negligible. The atmospheric density decreases by about 6 orders of magnitude over 100 km in altitude.

The density may be defined as $\rho(z)=\rho(0)\ e^{-az}$ for an isothermal atmosphere, where $a=g/R_a T$. Combining this expression for density with Eq. (12) then yields

$$\frac{\partial^2 p_s}{\partial t^2}=c^2\left(1+\mu\frac{\partial}{\partial t}\right)\nabla^2 p_s-\xi\frac{\partial p_s}{\partial t}+ac^2\frac{\partial p_s}{\partial z}. \tag{16}$$

The outgoing solution of Eq. (16) for a point source at the origin is given by the real part of

$$p_s(R,t)=Ae^{-az/2}\frac{e^{i\omega(R/c_p(\omega)\pm t)}}{R}e^{-\alpha(\omega)R}$$
$$=A\sqrt{\rho}\frac{e^{i\omega(R/c_p(\omega)\pm t)}}{R}e^{-\alpha(\omega)R}. \tag{17}$$

This expression is accurate for $\mu\omega\ll 1$ and $\omega\gg cg/R_a T$. The former requirement is accurate for infrasound frequencies and atmospheric viscosities. The latter requirement is valid at periods much less than 5 min, at which point buoyancy effects (gravity waves) are significant. Since the vertical pressure and density gradients depend on gravity, this may suggest that gravitational forces are significant in computing infrasound propagation. However, tests showed that inclusion of gravity terms within the equations governing linear acoustic propagation (e.g., Gill, 1982) led to waveforms that differed by less than 1% over propagation distances of 10 km at frequencies greater than 0.02 Hz. The effect of the density gradient on the wavenumber and velocity becomes significant at lower frequencies than are considered in this paper.

Comparison of Eqs. (14) and (16) indicates that pressure fluctuations in a medium with exponentially decreasing density attenuate more rapidly by a factor of $\sqrt{\rho}$ as they propagate upward, as compared to pressure fluctuations from a source in a uniform density medium. Conversely, the pressure amplitudes decrease less rapidly as the wave propagates downward into denser atmosphere. This follows from consideration of the energy density of the propagating wave (Gill, 1982). Note that that this is not an absorption effect since energy is not lost to the atmosphere.

C. FDTD equations

Though Eqs. (11) correctly describe the physics of acoustic propagation through an attenuating atmosphere, they are not in an optimal form for FDTD implementation. More conveniently, the first-order differential equations in time may be expressed as

$$\frac{\partial\mathbf{v}_s}{\partial t}=\mathbf{f}_i-\frac{1}{\rho}\left(1+\mu\frac{\partial}{\partial t}\right)\nabla p_s, \tag{18a}$$

and

$$\frac{\partial p_s}{\partial t}=-\rho c^2\nabla\cdot\mathbf{v}_s-\xi_s p. \tag{18b}$$

Combining these equations and omitting external forces yields the governing equation Eq. (12), assuming terms involving products of viscosity and density gradients are negligible. Note that, taken individually, Eqs. (18a) and (18b) are not equivalent to Eqs. (11), but combined, each set yields Eq. (12) to first order.

The FDTD approach is based on replacing the spatial and time derivatives in the governing equations by their difference approximations. The system of Eqs. (18a) and (18b) is solved here for two-dimensional (2D) models using a staggered-grid finite-difference technique originally proposed by Yee (1966). The model is divided into a grid of cells of dimension Δx by Δy, each with uniform density and velocity. The pressure variables are sampled at the center of each grid at times $n\Delta t$, where Δt is the temporal step size, and the velocity variables are sampled at points straddling the grid boundaries at times $(n+1/2)\Delta t$. Sampling points in this way yields discretized difference operators that are accurate to second order.

Adopting the notation

$$p_{I,J}^n=p_s(I\Delta x,J\Delta z,n\Delta t), \tag{19a}$$

$$v_{x,I,J}^{n+1/2}=v_{s,x}((I-1/2)\Delta x,J\Delta y,(n+1/2)\Delta t), \tag{19b}$$

$$v_{y,I,J}^{n+1/2}=v_{s,y}(I\Delta x,(J-1/2)\Delta y,(n+1/2)\Delta t), \tag{19c}$$

the set of ions Eqs. (18a) may be replaced by

$$\frac{v_{x,I,J}^{n+1/2}-v_{x,I,J}^{n-1/2}}{\Delta t}=-\frac{1}{\rho_{I-1/2,J}}\left[\left(1+\frac{\mu_{I-1/2,J}}{\Delta t}\right)\left(\frac{p_{I,J}^n-p_{I-1,J}^n}{\Delta x}\right)-\frac{\mu_{I-1/2,J}}{\Delta t}\left(\frac{p_{I,J}^{n-1}-p_{I-1,J}^{n-1}}{\Delta x}\right)\right], \tag{20a}$$

$$\frac{v_{y,I,J}^{n+1/2}-v_{y,I,J}^{n-1/2}}{\Delta t}=-\frac{1}{\rho_{I,J-1/2}}\left[\left(1+\frac{\mu_{I,J-1/2}}{\Delta t}\right)\left(\frac{p_{I,J}^n-p_{I,J-1}^n}{\Delta y}\right)-\frac{\mu_{I,J-1/2}}{\Delta t}\left(\frac{p_{I,J}^{n-1}-p_{I,J-1}^{n-1}}{\Delta y}\right)\right], \tag{20b}$$

where $\rho_{I,J}$ denotes the density, and $\mu_{I,J}$ the shear viscosity values at the center of the $[I,J]$th cell, and the half-integer subscripts denote the average values between two adjacent cells. The discretized version of Eq. (18b) is given by

$$\frac{p_{I,J}^{n+1}-p_{I,J}^{n}}{\Delta t}=-\rho_{I,J}c_{I,J}^{2}\left[\frac{v_{x,I+1,J}^{n+1/2}-v_{x,I,J}^{n+1/2}}{\Delta x}+\frac{v_{y,I,J+1}^{n+1/2}-v_{y,I,J}^{n+1/2}}{\Delta y}\right]-\xi_{I,J}\left[\frac{p_{I,J}^{n+1}+p_{I,J}^{n}}{2}\right]. \tag{21}$$

where $c_{I,J}$ and $\xi_{I,J}$ denote sound speeds and damping values within the $[I,J]$th cell. Equations (20a) and (20b) indicate that only one set of pressure variables p^n must be stored if the μ variable is equal to zero. Introduction of this attenuation coefficient requires saving an extra matrix of the pressure variables, i.e., p^{n-1}, at each time step. The reason for replacing Eqs. (11) with Eqs. (18a) and (18b) is now apparent; use of Eqs. (11) would require saving both the v_x^{n-1} and v_y^{n-1} matrices and would involve may more computational steps, thus increasing the computational load.

The term involving μ in Eq. (18a) is expressed as a backward difference operator in time in Eqs. (20), rather than a central difference operator; thus, it is accurate only to first order. The numerical errors resulting from this choice are examined more closely in the next subsection. The ξp term of Eq. (18b) is computed in Eq. (21) using the time average of the pressure terms at times n and $n+1$. The time derivative on the left-hand side of Eq. (21) is therefore correctly centered at time $n+1/2$.

Equation (21) may be rearranged as

$$p_{I,J}^{n+1}\left(1+\frac{\xi_{I,J}\Delta t}{2}\right)=p_{I,J}^{n}\left(1-\frac{\xi_{I,J}\Delta t}{2}\right)-\rho_{I,J}c_{I,J}^{2}\Delta t\left[\frac{v_{x,I+1,J}^{n+1/2}-v_{x,I,J}^{n+1/2}}{\Delta x}+\frac{v_{y,I,J+1}^{n+1/2}-v_{y,I,J}^{n+1/2}}{\Delta y}\right]. \tag{22}$$

The factor $(1\pm\xi\Delta t/2)$ in the above equation is a first-order Taylor approximation to $\exp[\pm\xi\Delta t/2]$. The update equations for the pressure p may then be expressed more accurately as

$$p_{I,J}^{n+1}=p_{I,J}^{n}e^{-\xi_{I,J}\Delta t}-\rho_{I,J}c_{I,J}^{2}\Delta t\left[\frac{v_{x_{I+1,J}}^{n+1/2}-v_{x_{I,J}}^{n+1/2}}{\Delta x}+\frac{v_{y_{I,J+1}}^{n+1/2}-v_{y_{I,J}}^{n+1/2}}{\Delta y}\right]e^{-\xi_{I,J}\Delta t/2}. \tag{23}$$

Equations (20a) and (20b), and Eq. (23) form the set of coupled equations used in the numerical implementation of the FDTD method.

D. Numerical dispersion and stability

Approximations made in discretizing the continuous partial differential equations lead to numerical dispersion in FDTD solutions (Taflove and Hagness, 2000). The degree of dispersion depends on the ratio of the propagating wavelength to the grid discretization. A rule of thumb for nonattenuating media is that there should be at least 10 nodes per wavelength for the staggered-grid FD method developed by Yee (1966). To compute numerical dispersion for the coupled equations Eqs. (20) and (23), one may consider an homogeneous medium with uniform density, sound speed, viscosity, and damping values. A trial FDTD set of solutions for the velocity and pressure fields of the form

$$V_{x,I,J}^{n+1/2}=V_{x0}e^{i(\omega(n+1/2)\Delta t-\tilde{k}_x(I-1/2)\Delta x-\tilde{k}_yJ\Delta y)}, \tag{24a}$$

$$V_{y,I,J}^{n+1/2}=V_{y0}e^{i(\omega(n+1/2)\Delta t-\tilde{k}_xI\Delta x-\tilde{k}_y(J-1/2)\Delta y)}, \tag{24b}$$

$$P_{I,J}^{n}=P_0e^{i(\omega n\Delta t-\tilde{k}_xI\Delta x-\tilde{k}_yJ\Delta y)}, \tag{24c}$$

may be postulated, where $\tilde{k}_x$ and $\tilde{k}_y$ are the numerical approximations to the horizontal and vertical wavenumbers.

Substitution of the trial wave solutions Eqs. (24a) and (24c) into Eq. (20a) yields the following relation:

$$V_{x0}=P_0\frac{\Delta t}{\rho\Delta x}\frac{\sin(\tilde{k}_x\Delta x/2)}{\sin(\omega\Delta t/2)}\left[1+\frac{\mu}{\Delta t}(1-e^{-i\omega\Delta t})\right]. \tag{25a}$$

Similarly, substituting Eqs. (24b) and (24c) into Eq. (20b) yields

$$V_{y0}=P_0\frac{\Delta t}{\rho\Delta y}\frac{\sin(\tilde{k}_y\Delta y/2)}{\sin(\omega\Delta t/2)}\left[1+\frac{\mu}{\Delta t}(1-e^{-i\omega\Delta t})\right]. \tag{25b}$$

Finally, the trial solutions for the partical velocities may be substituted into Eq. (23) to get

$$P_0\left[\frac{\sin(\omega\Delta t/2-i\xi\Delta t/2)}{\Delta t}\right]=\rho c^2\left[V_{x0}\frac{\sin(\tilde{k}_x\Delta x/2)}{\Delta x}+V_{y0}\frac{\sin(\tilde{k}_y\Delta y/2)}{\Delta y}\right]. \tag{26}$$

Equations (25a) and (25b) are substituted into Eq. (26) to yield a numerical dispersion relation. For the case where a square cell grid is used, i.e., $\Delta x=\Delta y=\Delta$, the numerical dispersion relation may be expressed as

$$\left(\frac{\Delta}{c\Delta t}\right)^2\left[\frac{\sin[(\omega-i\xi)\Delta t/2]\sin(\omega\Delta t/2)}{1+(\mu/\Delta t)(1-e^{-i\omega\Delta t})}\right]=\sin^2\left(\frac{\tilde{k}_x\Delta}{2}\right)+\sin^2\left(\frac{\tilde{k}_y\Delta}{2}\right). \tag{27}$$

The accuracy of the FDTD computations for a given time discretization Δt and grid spacing Δ can be determined using this equation. Defining the Courant stability factor $S=(c\Delta t/\Delta)$ and the grid sampling rate $N_\lambda=(\lambda/\Delta)$, the dispersion relation Eq. (27) may be reformulated as

$$\frac{1}{S^2}\left[\frac{\sin(\pi S/N_\lambda-i\xi\Delta t/2)\sin(\pi S/N_\lambda)}{1+(\mu/\Delta t)(1-e^{-i2\pi S/N_\lambda})}\right]=\sin^2\left(\frac{\Delta\tilde{k}\cos\theta}{2}\right)+\sin^2\left(\frac{\Delta\tilde{k}\sin\theta}{2}\right), \tag{28}$$

where θ is the propagation direction with respect to the x-axis. For $\mu=\xi=0$, this equation reduces to the numerical dispersion relation found in Taflove and Hagness (2000). Equation (28) shows that the numerical dispersion introduced by FD discretization is a function of the propagation

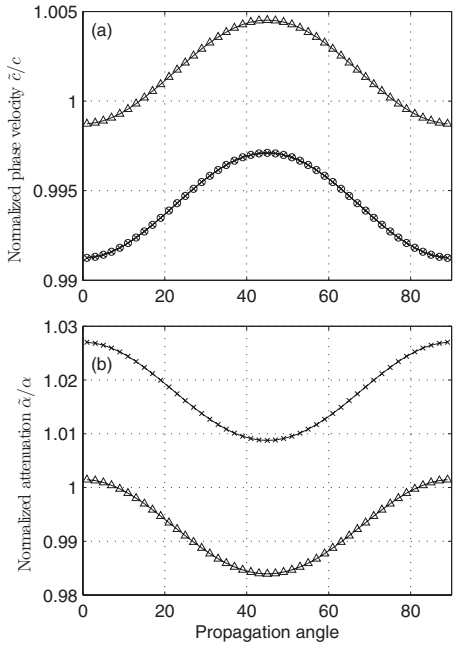

FIG. 4. (a) Variation of the numerical sound-speed ratio $\tilde{c}/c$ with propagation angle for models with no attenuation (circles); $\xi=0.01$, $\mu=0$ (x's); $\xi=0$, $\mu=0.005$ (triangles). The case $\xi=0.01$, $\mu=0$, produces negligibly more numerical dispersion than for the case of no attenuation. Propagation angles are with respect to the horizontal axis. (b) Variation of the attenuation ratios $\mathrm{Im}(\tilde{k})/\mathrm{Im}(k)$ for the models with nonzero attenuation as given above. $S=0.5$, $N_\lambda=12$, and $\Delta t=0.0167$ s were used for each case.

direction as well as the temporal and spatial sampling intervals.

For accurate FDTD simulation the grid sampling rate N_λ, and hence the time sampling rate, is based on the highest frequencies propagated through the grid. As an example, consider a model with sound speed $c=300$ m/s and a source bandwidth of up to 2.5 Hz. Setting $N_\lambda=12$ at the upper end of the frequency range yields a grid spacing of $\Delta=10$ m. A Courant stability factor $S=0.5$ yields a time sampling interval of $\Delta t=0.0167$ s. Figure 4(a) shows the normalized numerical sound speed $\tilde{c}/c=\omega_{\max}/\mathrm{Re}(\tilde{k})$ as a function of propagation angle for models with no attenuation (circles); $\xi=0.01$, $\mu=0$ (x's); $\xi=0$, $\mu=0.005$ (triangles). Figure 4(b) shows the normalized attenuation factors $\mathrm{Im}(-\tilde{k})/(\xi/(2c))$ and $\mathrm{Im}(-\tilde{k})/(\mu*\omega^2/(2c))$ for the latter two models. Note that the numerical phase velocity computed here differs from the dispersive velocities examined in Sec. III as it results from the discretization of the wave equations. Only in the case $\lim \Delta t\to 0$ and $\lim \Delta\to 0$, it can be shown that the numerical wavenumber $\tilde{k}^2$ approaches k^2 as defined by Eq. (4).

As indicated in Fig. 4, both the numerical phase velocity and attenuation depend weakly on the propagation angle; however, the difference is less than 2% for the given discretization values. Furthermore, variations in numerical phase velocities exists whether or not attenuation is included. For $\mu=0$, $\xi\neq 0$ the ξ value has minimal effect on the numerical phase velocity and attenuation over frequencies and attenuation values relevant to global infrasound propagation. However, for $\xi=0$, $\mu\neq 0$, the accuracy of the FDTD solution

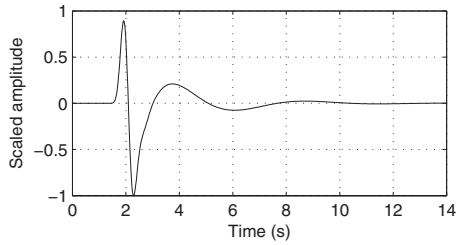

FIG. 5. The source function used for examples A, B, and C. This source was generated by bandpass filtering a spikelike waveform between 0.02 and 2.2 Hz.

degrades with increasing μ values—the normalized velocities increase and the normalized attenuation factors decrease.

Finally, it is known that for a 2D model the time step Δt must be chosen such that $S<1/\sqrt{2}$ to ensure stability (Taflove and Hagness, 2000). Neglecting ξ, it can be shown that for $\omega_{\max}\mu\ll 1$, the stability requirement is given by

$$\Delta t<\frac{\Delta}{\sqrt{2}c(1+\omega_{\max}^2\mu^2/4)}. \tag{29}$$

The conditions $\omega_{\max}\mu\ll 1$ and Eq. (29) provide stability limits on the computations. Thus, the requirement $\omega_{\max}\mu\ll 1$ imposes an upper limit on μ or, conversely, on $\omega_{\max}$ for FDTD computations.

V. EXAMPLES

Several FDTD solutions to problems of infrasound propagation through an absorbing atmosphere are presented in this section. Examples A and B are idealized problems used to test and illustrate the effects of including attenuation coefficients in the FDTD method. Example C involves a more realistic atmospheric waveguide. For each example the side and top boundaries are terminated using a perfectly matched layer (PML) absorbing boundary condition (Berenger, 1994) initially developed for electromagnetic waves. The PML boundary conditions are also applied to the bottom boundary for examples A and B, that is, the models are assumed to be whole spaces. The source function shown in Fig. 5, which consists of a high-frequency pulse followed by a lower-frequency wave, was used for each example.

Example A consists of a uniform whole space with constant density and a constant sound speed of 330 m/s. Pressure waves are sampled at distances from 2 to 10 km from the source, at intervals of 2 km. The node spacing is 10 m, yielding 15 nodes per wavelength at the maximum source frequency of 2.2 Hz, and the time sampling interval is 0.0168 s, corresponding to $S=1/1.8$. Results were synthesized for a model with no attenuation and compared to three attenuation models: first, a model with constant attenuation values of $\xi=0$, $\mu=0.002$; from Eq. (10a), this corresponds to an attenuation coefficient of $1.039\times 10^{-3}\ f^2$ dB/m; second, a model with constant attenuation values of $\xi=0$, $\mu=0.005$, corresponding to an attenuation coefficient of $2.60\times 10^{-3}\ f^2$ dB/m; and third, a model with $\xi=0.01$, $\mu=0$; from Eq. (10b), this corresponds to an attenuation coefficient of 1.316×10^{-4} dB/m.

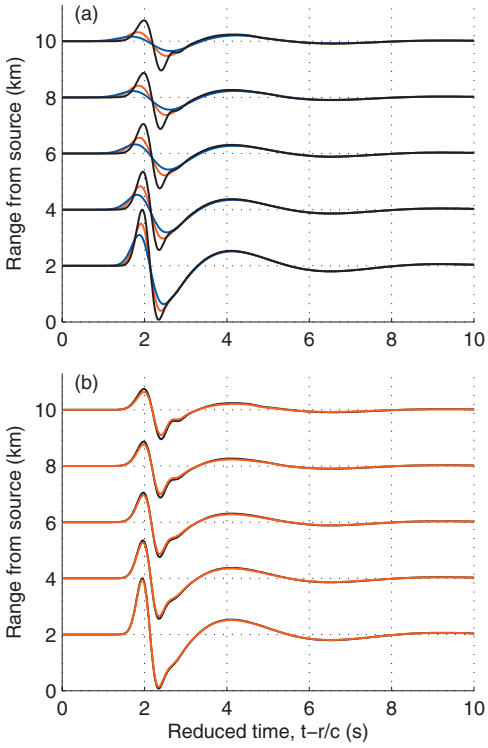

FIG. 6. (a) Synthesized waveforms for models with varying μ values at distances from 2 to 10 km from the source. The pressure waveforms are shown as a function of reduced time, which is the time minus the range divided by the sound speed (c=330 m/s). The waveforms for the models with no attenuation are shown by the black line; the results for μ=0.002 are indicated in red, and the results for μ=0.005 are indicated in blue. (b) The black line shows the pressure solutions for the model with no attenuation; the red lines indicates waveforms corresponding to models with ξ=0.01.

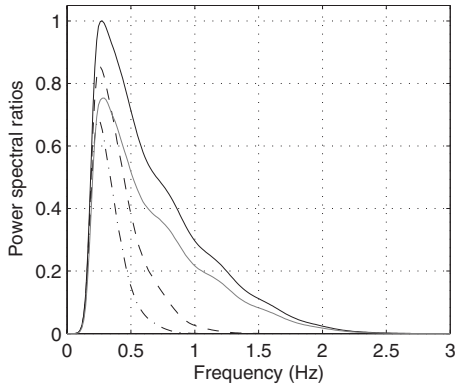

FIG. 7. Ratios of power spectra for pressure waveforms at a distance of 10 km from the source for example A. Power spectra are normalized with respect to the peak power of the waveform for the model with no attenuation (solid black line). The dashed line corresponds to the ξ=0, μ=0.002 model, the dash-dot line corresponds to the ξ=0, μ=0.005 model, and the gray line corresponds to the ξ=0.01, μ=0 model.

The synthesized waveforms for models with varying μ are shown in Fig. 6(a). The waveforms for models with no attenuation show two-dimensional geometrical spreading away from the source. In comparison, waveforms propagated through models with nonzero μ values show greater attenuation of the initial higher frequency pulse, but the later, low-frequency wave at approximately 4 s is virtually unchanged. Furthermore, the waveforms for the nonzero μ models are slightly advanced with respect to the nonattenuated waveforms. The numerical dispersion relation, Eq. (28), predicts that the phase velocity for the model with μ=0.005 should be about 0.5% faster than the model with no attenuation, as shown in Fig. 4(a), and in agreement with Eq. (7a), which also predicts higher phase velocities with increasing μ. Synthesized waveforms for models with no attenuation are almost identical to those for the model with ξ=0.01, as shown in Fig. 6(b). This is approximately the highest value of the constant attenuation coefficient ξ realized in the Earth's atmosphere, as indicated in Fig. 2. As shown in Fig. 6(b), the constant attenuation term conserves the shape of the waveform.

The power spectra for the pressure waveforms sampled at a distance of 10 km from the source are shown in Fig. 7. As indicated, waveforms for models with $\mu \neq 0$ are most significantly attenuated at the highest frequencies sampled, whereas waveforms for models with $\xi \neq 0$ are uniformly attenuated at all frequencies. For ξ=0.01 the power spectral ratio of attenuated to unattenuated waveforms at 10 km is 0.736 for the entire source bandwidth, corresponding to a transmission loss of 1.33 dB; this agrees to within 1% with the predicted transmission loss of 1.32 dB at 10 km for this value. ξ value. For the μ=0.002 model, the attenuation at a frequency of 0.25 Hz is 0.629 dB, which compares well with the predicted transmission loss of 0.631 dB at this distance and frequency. Similarly, the attenuation for the μ=0.005 model, observed to be 1.57 dB at 0.25 Hz and 10 km from the source, compares well with the predicted transmission loss of 1.58 dB.

The model for example B is similar to example A with the difference that the atmospheric density decreases exponentially with altitude at a rate of three orders of magnitude over 50 km. Pressure waves are sampled at altitudes from 2 to 8 km both above and below the source, at intervals of 2 km. Waveforms were synthesized twice; once for a model with no attenuation and once for a model with ξ=0, μ=0.002, as shown in Fig. 8. Comparing this to Fig. 6(a), it may be seen that waveform amplitudes decrease more rapidly with increasing distance from the source as they propagate upward into thinner atmosphere than for a model with constant density. Conversely, the waveform's amplitudes decrease much more slowly as the acoustic energy propagates downward. Again, including a nonzero μ term in the model leads to waveforms with suppressed high-frequency pulses.

Normalized power spectra for each waveform are shown in Fig. 9. The power spectra corresponding to the model with μ=0.002 lie along diminishing curves as the distance from the source increases. The transmission loss values of 0.148, 0.284, 0.428, and 0.576 dB for the synthesized waveforms at the peak frequency of 0.26 Hz compare well with the predicted transmission loss values of 0.142, 0.283, 0.425, and 0.566 dB at this frequency.

Example C is similar to example B except that both realistic sound-speed and attenuation profiles for an altitude range of 89 to 111 km are used, as shown in Fig. 2. The source is located at an altitude of 100 km and waveforms are sampled at altitudes from 2 to 8 km above and below the source, at intervals of 2 km. Since the sound speeds are

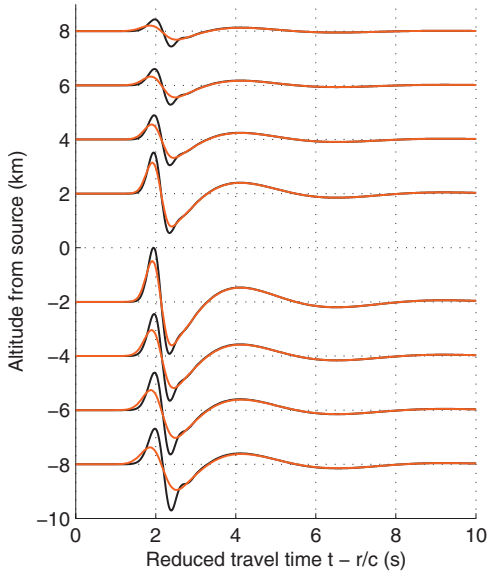

FIG. 8. Synthesized pressure waveforms for example B at distances from 2 to 8 km above (upper waveforms) and below the source located at 0 km (lower waveforms), shown as a function of reduced time. Results for a model with no attenuation are shown in black and results for a model with $\mu=0.002$ are shown in red.

lower for this final example, the model was discretized in cells of 8 m $\times$ 8 m and the time sampling interval was set to 0.0135 s. Waveforms were synthesized both with and without attenuation. Results are shown in Fig. 10. Arrivals are earlier for upward propagation due to variations in the sound-speed profiles, as shown in Fig. 2.

As indicated in Fig. 10, the high frequencies are more severely attenuated as they propagate upward from the source rather than downward, since the atmospheric absorption increases with altitude. This is seen more clearly in Fig. 11, where the normalized power spectra for each attenuated waveform are compared to the corresponding nonattenuated

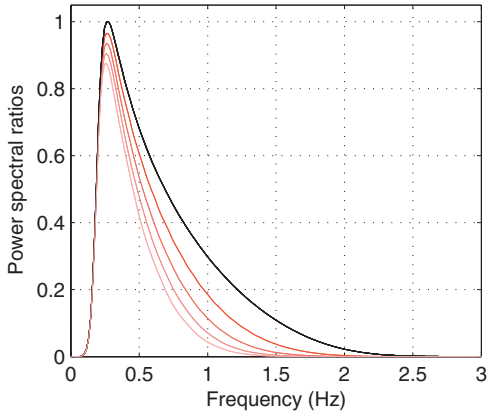

FIG. 9. Normalized power spectra for each waveform shown in Fig. 8. At each range step, the power spectra are normalized with respect to the peak power for waveforms propagated through the nonabsorbing medium. Power spectra for the waveforms synthesized from the model with no attenuation lie along a single curve, shown by the heavy line, indicating that spectral content is preserved. The red lines, which become lighter with increasing distance from the source, are the normalized power spectra for waveforms at distances of 2, 4, 6, and 8 km from the source for a model with $\mu=0.002$. The red lines show that high frequencies are diminished with increasing distance from the source.

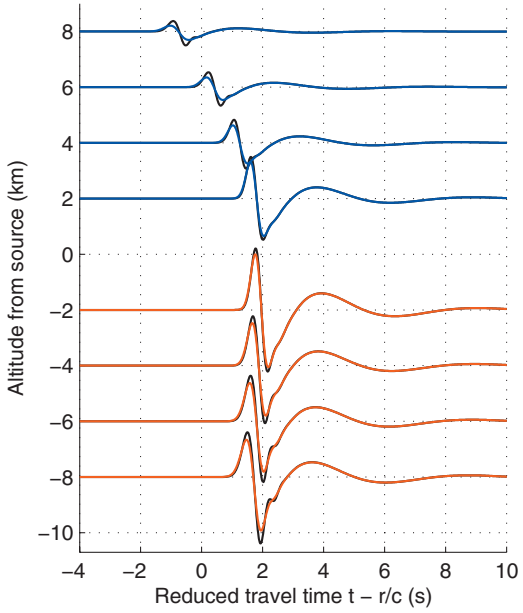

FIG. 10. Synthesized pressure waveforms for example C at distances from 2 to 8 km above and below the source located at 100 km. Results for a model with no attenuation are shown in black and results for a model with realistic attenuation profiles for this altitude range are shown in red for down-going waves and blue for up-going waves. The reducing velocity was set to 260 m/s.

waveforms. As in Example B, the power spectra for waveforms lie along diminishing curves with increasing distance from the source, but here the attenuation is greater for the receivers above the source.

VI. DISCUSSION AND CONCLUSIONS

A FDTD technique has been developed for acoustic propagation through a heterogeneous absorbing atmosphere. The attenuation terms used in the propagation modeling were defined in such a way as to match observed variations in absorption with frequency. It was demonstrated that, for fre-

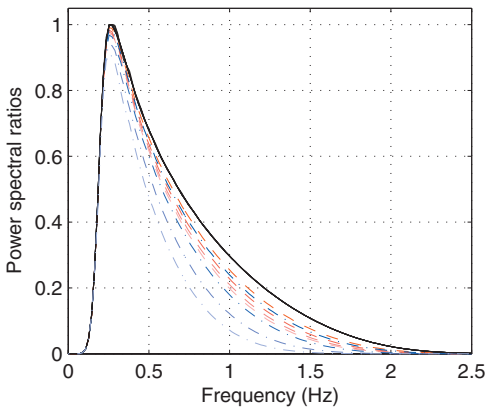

FIG. 11. Normalized power spectra for each waveform shown in Fig. 10. At each range step, the power spectra are normalized with respect to the peak power for waveforms propagated through a nonabsorbing medium. Power spectra for waveforms synthesized from the model with no attenuation lie along a single curve, shown by the black heavy line. The red dashed lines are the corresponding power spectra for down-going waves at distances of 2, 4, 6, and 8 km from the source and the blue dash-dotted lines are for up-going waves. Waveforms undergo greater attenuation for upward propagation than for downward propagation.

quency bandwidths of approximately two orders of magnitude, infrasound attenuation within the atmosphere may be modeled as the sum of a constant term β, and another term γ multiplied by the square of the frequency. For infrasound propagation within Earth's atmosphere, the former term dominates at altitudes of approximately 30–50 km, i.e., within the upper stratosphere; the μ term dominates at other altitudes.

Inclusion of attenuation terms in the wave equation is associated with some velocity dispersion, i.e., the sound velocity becomes a function of frequency. However, this effect is small except at very high attenuation levels within the upper atmosphere, and at the upper end of the frequency range of interest.

The accuracy of the absorbing FDTD technique was tested for several problems involving models with uniform velocity. By comparing results for models with and without attenuation terms, it was shown that the predicted transmission losses for the attenuating media agreed with those computed from the synthesized waveforms. Inclusion of the constant attenuation term does not reduce the stability or computation time of the algorithm. However, inclusion of the $\mu \neq 0$ term increases the computation time by approximately 50% and requires storage of an extra pressure time step. It also imposes extra conditions on the product of the frequency and viscosity, $\omega_{\max} \mu_{\max} \ll 1$, and on the temporal sampling interval $\Delta t < \Delta / [\sqrt{2} c (1 + \omega_{\max}^2 \mu^2 / 4)]$; these conditions are required to maintain stability of the two-dimensional FDTD algorithm. Note that the best-fit $\mu(z)$ profile depends on the frequency bandwidth of interest and decreases at higher frequency ranges; thus, this requirement does not preclude the use of this algorithm at higher frequencies.

Possible extensions of this work involve including terms in the wave equations to account for wind and gravitational effects. Wind affects infrasound propagation at all frequencies; gravitational effects could alter the waveform solutions at lower frequencies than are of interest here. Other extensions include testing the accuracy of the Sutherland and Bass (2004) models by comparing numerically synthesized waveforms derived from the algorithm presented here against experimental observations.

ACKNOWLEDGMENTS

Thanks to Claus Hetzer and Hank Bass of the National Center of Physical Acoustics at the University of Mississippi for providing their code to compute attenuation coefficients as a function of frequency and altitude. This work was supported by UM Subcontract No. 07-08-013. Distribution A. Approved for Public Release; distribution unlimited. Finally, thanks to three anonymous reviewers for their careful reviews. Their recommendations for improving the manuscript are sincerely appreciated.

APPENDIX: ACOUSTIC PROPAGATION IN A VISCOUS FLUID

The equations governing linear acoustic propagation through an attenuating fluid or gas may be derived as outlined in this Appendix.

The equation of motion relating the fluid acceleration to the stress tensor σ_{ij} and the external volume force per unit mass f_i is given by

$$\rho \frac{Dv_i}{Dt} = \rho f_i + \frac{\partial \sigma_{ij}}{\partial x_j}, \tag{A1}$$

(Eq. 3.2.2 of Batchelor, 1967) where ρ denotes the density, v_i is the particle velocity, and D/Dt is the advective derivative, $D/Dt = \partial/\partial t + \mathbf{v} \cdot \boldsymbol{\nabla}$.

A Newtonian fluid is one in which the shear stress is linearly proportional to the rate of shear deformation. In this case the stress-strain relationship in summation notation is given by

$$\sigma_{ij} = -p \delta_{ij} + A_{ijkl} \frac{\partial v_k}{\partial x_l}, \tag{A2}$$

(Eq. 7.3-1 of Fung, 1977) where p is the mean normal stress, δ_{ij} is the Kronecker delta, equal to 1 if $i=j$ and 0 otherwise, and the fourth-order tensor coefficients A_{ijkl} depend on the state of the fluid, i.e., the temperature, but not on the stress or rate of deformation. The second term on the right represents the deviatoric stress tensor and is defined such that the diagonal terms sum to zero. The stress tensor may be expressed as

$$\sigma_{ij} = -p \delta_{ij} + 2\mu' (e_{ij} - 1/3 \boldsymbol{\Delta} \delta_{ij}), \tag{A3}$$

if the fluid is isotropic (Eq. 3.2.11 of Batchelor, 1967; Eq. 7.3.6 of Fung, 1977), where μ' is the viscosity in units of kg m^{-1} s^{-1}, $e_{ij} = 1/2(\partial v_i/\partial x_j + \partial v_j/\partial x_i)$, and $\boldsymbol{\Delta}$ is the rate of expansion given by $\boldsymbol{\Delta} = \boldsymbol{\nabla} \cdot \mathbf{v} = e_{kk}$. A fluid with behavior that obeys Eq. (A3) is called a Stokes' fluid.

Substitution of Eq. (A3) for the stress tensor into Eq. (A1) yields the following equation of motion for a Stokes' fluid:

$$\rho \frac{Dv_i}{Dt} = \rho f_i - \frac{\partial p}{\partial x_i} + \mu' \left(\boldsymbol{\nabla}^2 v_i + \frac{1}{3} \frac{\partial \boldsymbol{\Delta}}{\partial x_i} \right). \tag{A4}$$

As discussed in Batchelor (1967), Eqs. (A3), and hence Eq. (A4), were derived under the assumption that the rate of isotropic expansion does not contribute to the stress; thus, the mean normal stress p is equal to the pressure. If a damping term is added the equation of motion as an external force, Eq. (A4) becomes

$$\rho \frac{Dv_i}{Dt} = \rho f_i - \frac{\partial p}{\partial x_i} + \mu' \left(\boldsymbol{\nabla}^2 v_i + \frac{1}{3} \frac{\partial \boldsymbol{\Delta}}{\partial x_i} \right) - \xi' v_i, \tag{A5}$$

where ξ' is the damping coefficient in units of kg m^{-3} s^{-1}. The inclusion of this term is entirely heuristic and is used to provide an additional degree of freedom to the governing equations and thus provide a better fit with observed attenuation values, particularly at midaltitudes. Gravitational effects may also be included as an external force but are ne-

glected here as they are relevant to much lower frequencies than are dealt with in this paper.

In the presence of fluctuations caused by the passage of a sound wave, the total pressure, density, and velocity may be expressed as $p=p_o+p_s$, $v=w+v_s$, and $\rho=\rho_o+\rho_s$, where p_o, w, and ρ_o are ambient values, and p_s, v_s, and ρ_s are small fluctuations caused by the sound wave. A linear expression for the particle velocity in the presence of a sound wave may be derived by inserting these values into Eq. (A5), and retaining only first-order terms in the pressure, velocity, and density terms. Furthermore, the effects of wind are neglected in this paper. Then,

$$\frac{\partial v_{s,i}}{\partial t}=f_i-\frac{1}{\rho_o}\left[\frac{\partial p_s}{\partial x_i}-\mu'\left(\nabla^2 v_{s,i}+\frac{1}{3}\frac{\partial \Delta_s}{\partial x_i}\right)+\xi' v_{s,i}\right], \quad \text{(A6)}$$

where $\Delta_s=\nabla\cdot\mathbf{v}_s$. In vector notation, this may be written as

$$\frac{\partial \mathbf{v}_s}{\partial t}=\mathbf{f}_i-\frac{1}{\rho_o}\left[\nabla p_s-\mu'\left(\nabla^2\mathbf{v}_s+\frac{1}{3}\nabla(\nabla\cdot\mathbf{v}_s)\right)+\xi'\mathbf{v}_s\right], \quad \text{(A7)}$$

where $\nabla^2\mathbf{v}_s$ is a vector with components $\nabla^2\mathbf{v}_s=(\nabla^2\mathbf{v}_{s,x},\nabla^2\mathbf{v}_{s,y},\nabla^2\mathbf{v}_{s,z})$. Viscosity values μ' are nearly constant within the atmosphere up to an altitude of 86 km (Gill, 1982).

The equation of state for air is given by $p=p(\rho,S)$, where S is the entropy. Applying the advective derivative to the equation of state yields

$$\frac{Dp}{Dt}=\tilde{c}^2\frac{D\rho}{Dt}+h\frac{DS}{Dt}, \quad \text{(A8)}$$

where $\tilde{c}^2=\partial p/\partial\rho$ is the squared sound speed in the presence of a sound wave, and $h=\partial p/\partial S$. The first term on the right denotes the change in pressure associated with a density change. The second term represents the increase in entropy caused by the passage of a sound wave, and is associated with an increase in temperature due to viscous dissipation. In the absence of a mass source, the conservation of mass equation is given by

$$\frac{D\rho}{Dt}=-\rho\nabla\cdot\mathbf{v}, \quad \text{(A9)}$$

so the first term on the right of Eq. (A8) is given by $-\rho\tilde{c}^2\nabla\cdot\mathbf{v}$.

The entropy per unit mass η is related to the internal energy per unit mass E through

$$Td\eta=dE+pd(1/\rho), \quad \text{(A10)}$$

(Eq. 3.2.1 of Gill, 1982), where T is the temperature. Applying the advective derivative leads to

$$T\frac{D\eta}{Dt}=\frac{DE}{Dt}-\frac{p}{\rho^2}\frac{D\rho}{Dt}. \quad \text{(A11)}$$

Using the equation for the conservation of mass leads to

$$T\frac{D\eta}{Dt}=\frac{DE}{Dt}+\frac{p}{\rho}\nabla\cdot\mathbf{v}. \quad \text{(A12)}$$

From Eq. (3.4.4) of Batchelor (1967),

$$\frac{DE}{Dt}=-\frac{p}{\rho}\nabla\cdot\mathbf{v}+\frac{2\mu}{\rho}\left(e_{ij}e_{ij}-\frac{1}{3}(\nabla\cdot\mathbf{v})^2\right)+\frac{1}{\rho}\frac{\partial}{\partial x_i}\left(k\frac{\partial T}{\partial x_i},\right), \quad \text{(A13)}$$

where the first term on the right is related to compression or expansion, the second term relates to the shear viscosity, and the final term relates to heat exchange by molecular conduction, which is not considered further. Combining Eqs. (A12) and (A13) (neglecting the conduction term) leads to

$$T\frac{D\eta}{Dt}=\frac{2\mu}{\rho}\left(e_{ij}e_{ij}-\frac{1}{3}(\nabla\cdot\mathbf{v})^2\right). \quad \text{(A14)}$$

The change in the entropy per unit mass is proportional to the square of the particle velocity perturbation in the absence of wind, and is thus negligible to first order for linear propagation and for small μ.

Since propagation is isentropic to first order, the second term of Eq. (A8) may be neglected. It may also be shown that for small perturbations $\tilde{c}^2=c^2$ (e.g., Gill, 1982), where $c^2=\partial p_o/\partial\rho_o$ is the squared static sound speed. Then, combining Eqs. (A8) and (A9) and retaining only first-order terms leads to the following equation for pressure fluctuations due to a sound wave:

$$\frac{\partial p_s}{\partial t}=-\rho_o c^2\nabla\cdot\mathbf{v}_s, \quad \text{(A15)}$$

where pressure gradients have been neglected. Equations (A7) and (A15) form a complete set of equations describing linear acoustic propagation through an attenuating fluid or gas.

Applying the operator $\partial/\partial t$ to Eq. (A15) and making use of Eq. (A7) yields the second-order equation for p_s,

$$\frac{\partial^2 p_s}{\partial t^2}=c^2[\nabla^2 p_s-4\mu'/3\nabla^2(\nabla\cdot v_s)+\xi'(\nabla\cdot v_s)]-\frac{c^2}{\rho_o}\nabla\rho_o\cdot\nabla p_s+O\left(\rho_o\nabla\left(\frac{\mu'}{\rho_o}\right)\right)+O\left(\rho_o\nabla\left(\frac{\xi'}{\rho_o}\right)\right) \quad \text{(A16)}$$

where the external force f_i is omitted, and the identity $\nabla\cdot\nabla^2\mathbf{v}_s=\nabla^2(\nabla\cdot\mathbf{v}_s)$ has been used. The final two terms relate to gradients of the viscosity divided by the atmospheric density. These terms may be omitted for realistic atmospheric density and viscosity values. So, making use of Eq. (A15), Eq. (A16) may be expressed as

$$\frac{\partial^2 p_s}{\partial t^2}=c^2\left[1+\mu\frac{\partial}{\partial t}\right]\nabla^2 p_s-\xi\frac{\partial p}{\partial t}-\frac{c^2}{\rho_o}\nabla\rho_o\cdot\nabla p_s, \quad \text{(A17)}$$

where

$$\mu=4\mu'/(3\rho_o c^2);\quad \xi=\xi'/\rho_o, \quad \text{(A18)}$$

so that μ is in units of seconds, and ξ is in units of s^{-1}. Equation (A17) is the governing equation for acoustic propagation through an attenuating atmosphere, although it may be

noted that the inclusion of the term involving ξ was heuristic, used only to yield more realistic atmospheric absorption values.

Aki, K., and Richards, P. G. (**1980**). *Quantitative Seismology: Theory and Methods*, (W. H. Freeman and Co., San Francisco), Vol. **1**.

Arrowsmith, S. J., and Hedlin, M. A. H. (**2005**). "Observations of infrasound from surf in southern California," Geophys. Res. Lett. **32**, L09810.

Bass, H. E., Sutherland, L. C., Zuckerwar, A. J., Blackstock, D. T., and Hester, D. M. (**1995**). "Atmospheric absorption of sound: Further developments," J. Acoust. Soc. Am. **97**, 680–683.

Bass, H. E., Hetzer, C. H., and Raspet, R. (**2007**). "On the speed of sound in the atmosphere as a function of altitude and frequency," J. Geophys. Res. **112**, D15110.

Bass, H., Bhattacharyya, J., Garces, M., Hedlin, M. A. H., Olson, J., and Woodward, R. (**2006**). "Infrasound," Acoust. Today **2**, 9–19.

Batchelor, G. K. (**1967**). *An Introduction to Fluid Dynamics* (University Printing House, Cambridge).

Berenger, J. P. (**1994**). "A perfectly matched layer for the absorption of electromagnetic waves," J. Comput. Phys. **114**, 1185–1200.

Blanch, J. O., Robertsson, J. O. A., and Symes, W. W. (**1995**). "Modeling of a constant Q: Method and algorithm for an efficient and optimally inexpensive viscoelastic technique," Geophysics **60**, 176–184.

Botteldoren, D. (**1994**). "Acoustical finite-difference time-domain simulation in a quasi-Cartesian grid," J. Acoust. Soc. Am. **95**, 2213–2219.

Boyce, W. E., and DiPrima, R. C. (**1977**). *Elementary Differential Equations and Boundary Values Problems*, 3rd ed., (Wiley and Sons, Toronto).

Dain, Y., and Lueptow, R. M. (**2001**). "Acoustic attenuation in a three-gas mixture: Results," J. Acoust. Soc. Am. **110**, 2974–2979.

Day, S. M. (**1998**). "Efficient simulation of constant Q using coarse-grained memory variables," Bull. Seismol. Soc. Am. **88**, 1051–1062.

Day, S. M., and Minster, J. B. (**1984**). "Numerical simulation of attenuated wavefields using a Padé approximant method," Geophys. J. R. Astron. Soc. **78**, 105–118.

Der, Z. A., Shumway, R. H., and Herrin, E. T. (**2002**). *Monitoring the Comprehensive Nuclear-Test-Ban Treaty: Data Processing and Infrasound*, Pageoph Topical Volumes (Birkhuser, Basel).

Ejakov, S. G., Phillips, S., Dain, Y., Lueptow, R. M., and Visser, J. H. (**2003**). "Acoustic attenuation in gas mixtures with nitrogen: Experimental data and calculations," J. Acoust. Soc. Am. **113**, 1871–1879.

Emmerich, H., and Korn, M. (**1987**). "Incorporation of attenuation into time-domain computations of seismic wave fields," Geophysics **52**, 1252–1264.

Evans, L. B., Bass, H. E., and Sutherland, L. C. (**1972**). "Atmospheric absorption of sound: Theoretical predictions," J. Acoust. Soc. Am. **51**, 1565–1575.

Fung,Y. C. (**1977**). *A First Course in Continuum Mechanics*, 2nd ed. (Prentice-Hall, Inc., Englewood Cliffs, NJ).

Garceś, M., Willis, M., Hetzer, C., and Drob, D. (**2004a**). "On using ocean swells for continuous infrasonic measurements of winds in the lower, middle, and upper atmosphere," Geophys. Res. Lett. **31**, L19304.

Garceś, M., Bass, H., Drob, D., Hetzer, C., Hedlin, M., Le Pichon, A., Lindquist, K., North, R., and Olson, J. (**2004b**). "Forensic studies of infrasound from massive hypersonic sources," EOS (Wash. D.C.) **85** (43), 433–440.

Gill, A. E. (**1982**). *Atmosphere-Ocean Dynamics* (Academic, San Diego).

Jensen, F. B., Kuperman, W. A., Porter, M. B., and Schmidt, H. (**1994**). *Computational Ocean Acoustics* (AIP, Woodbury, NY).

Knopoff, L. (**1956**). "The seismic pulse in materials possessing solid friction. I. Plane waves," Bull. Seismol. Soc. Am. **46**, 175–183.

Le Pichon, A., Herry, P., Mialle, P., Vergoz, J., Brachet, N., Garceś, M., Drob, D., and Ceranna, L. (**2005**). "Infrasound associated with 2004–2005 large Sumatra earthquakes and tsunami," Geophys. Res. Lett. **32**, L19802.

Le Pichon, A., Garceś, M., Blanc, E., Barthelémy, M., and Drob, D. P. (**2002**). "Acoustic propagation and atmosphere characteristics derived from infrasonic waves generated by the Concorde," J. Acoust. Soc. Am. **111**, 629–641.

Lighthill, J. (**1978**). *Waves in Fluids* (Cambridge University Press, Cambridge, UK).

Lingevitch, J. F., Collins, M. D., and Siegmann, W. L. (**1999**). "Parabolic equations for gravity and acousto-gravity waves," J. Acoust. Soc. Am. **105**, 3049–3056.

Mikumo, T. (**1968**). "Atmospheric pressure waves and tectonic deformation associated with the Alaskan earthquake of March 28, 1964," J. Geophys. Res. **73**, 2009–2025.

Ostashev, V. E., Wilson, D. K., Liu, L., Aldridge, D. F., Symons, N. P., and Marlin, D. (**2005**). "Equations for finite-difference, time-domain simulation of sound propagation in moving inhomogeneous media and numerical implementation," J. Acoust. Soc. Am. **117**, 503–517.

ReVelle, D. O., Brown, P. G., and Spurny, P. (**2004**). "Entry dynamics and acoustics/infrasonic/seismic analysis for the Neuschwanstein meteorite fall," Meteorit. Planet. Sci. **39**, 1605–1625.

Sutherland, L. C., and Bass, H. E. (**2004**). "Atmospheric absorption in the atmosphere up to 160 km," J. Acoust. Soc. Am. **115**, 1012–1032.

Sutherland, L. C., and Bass, H. E. (**2006**). "Erratum: Atmospheric absorption in the atmosphere up to 160 km," J. Acoust. Soc. Am. **120**, 2985.

Taflove, A., and Hagness, S. C. (**2000**). *Computational Electrodynamics: The Finite-Difference Time-Domain Method*, 2nd ed. (Artech House, Norwood, MA).

Wilson, C. R., and Forbes, R. B. (**1969**). "Infrasonic waves from Alaskan volcanic eruption," J. Geophys. Res. **74**, 4511–4522.

Yee, K. S. (**1966**). "Numerical solution of initial boundary value problems involving Maxwell's equations in isotropic media," IEEE Trans. Antennas Propag. **14**, 302–307.

Young, J. M., and Greene, G. E. (**1982**). "Anomalous infrasound generated by the Alaskan earthquake of March 28, 1964," J. Acoust. Soc. Am. **71**, 334–339.